



**HAL**  
open science

## Plasticity of the dense hydrous magnesium silicate phase A at subduction zones conditions

K. Gouriet, N. Hilaret, E. Amiguet, N. Bolfan-Casanova, Y. Wang, Bruno  
Reynard, P. Cordier

### ► To cite this version:

K. Gouriet, N. Hilaret, E. Amiguet, N. Bolfan-Casanova, Y. Wang, et al.. Plasticity of the dense hydrous magnesium silicate phase A at subduction zones conditions. *Physics of the Earth and Planetary Interiors*, 2015, 248, pp.1-11. 10.1016/j.pepi.2015.09.004 . hal-02107591

**HAL Id: hal-02107591**

**<https://hal.science/hal-02107591>**

Submitted on 26 Nov 2020

**HAL** is a multi-disciplinary open access archive for the deposit and dissemination of scientific research documents, whether they are published or not. The documents may come from teaching and research institutions in France or abroad, or from public or private research centers.

L'archive ouverte pluridisciplinaire **HAL**, est destinée au dépôt et à la diffusion de documents scientifiques de niveau recherche, publiés ou non, émanant des établissements d'enseignement et de recherche français ou étrangers, des laboratoires publics ou privés.



Distributed under a Creative Commons Attribution - NoDerivatives 4.0 International License



## Plasticity of the dense hydrous magnesium silicate phase A at subduction zones conditions



K. Gouriet<sup>a,\*</sup>, N. Hilairot<sup>a</sup>, E. Amiguet<sup>b,c</sup>, N. Bolfan-Casanova<sup>d</sup>, Y. Wang<sup>e</sup>, B. Reynard<sup>b</sup>, P. Cordier<sup>a</sup>

<sup>a</sup> Unité Matériaux et Transformation, UMR 8207, CNRS – Université Lille 1, ENSCL, Villeneuve d'Ascq, France

<sup>b</sup> Laboratoire de Géologie de Lyon, Terre, Planètes et Environnement, Université de Lyon, CNRS, ENS de Lyon, Université Claude Bernard Lyon 1, Lyon, France

<sup>c</sup> Institute of Condensed Matter Physics, Ecole Polytechnique Fédérale de Lausanne, EPFL, Lausanne, Switzerland

<sup>d</sup> Laboratoire Magmas et Volcans, CNRS, 5, rue Kessler, 63000 Clermont-Ferrand, France

<sup>e</sup> Center for Advanced Radiation Sources, The University of Chicago, 5640 S. Ellis Avenue, Chicago, IL 60637, USA

### ARTICLE INFO

#### Article history:

Received 7 April 2015

Received in revised form 23 July 2015

Accepted 3 September 2015

Available online 12 September 2015

#### Keywords:

DHMS

Phase A

Dislocations

Glide plane

Dissociation

High pressure

Anisotropie

Peierls–Nabarro method

Generalized stacking faults

### ABSTRACT

The plasticity of the dense hydrous magnesium silicate (DHMS) phase A, a key hydrous mineral within cold subduction zones, was investigated by two complementary approaches: high-pressure deformation experiments and computational methods. The deformation experiments were carried out at 11 GPa, 400 and 580 °C, with *in situ* measurements of stress, strain and lattice preferred orientations (LPO). Based on viscoplastic self-consistent modeling (VPSC) of the observed LPO, the deformation mechanisms at 580 °C are consistent with glide on the (0001) basal and (0110) prismatic planes. At 400 °C the deformation mechanisms involve glide on (2110) prismatic, (0001) basal and {1121} pyramidal planes. Both give flow stresses of 2.5–3 GPa at strain rates of  $2\text{--}4 \times 10^{-5} \text{ s}^{-1}$ . We use the Peierls–Nabarro–Galerkin (PNG) approach, relying on first-principles calculations of generalized stacking fault ( $\gamma$ -surface), and model the core structure of potential dislocations in basal and prismatic planes. The computations show multiple dissociations of the  $\frac{1}{3}[2\bar{1}\bar{1}0]$  and  $[0\bar{1}\bar{1}0]$  dislocations ( $\langle a \rangle$  and  $\langle b \rangle$  dislocations) in the basal plane, which is compatible with the ubiquity of basal slip in the experiments. The  $\gamma$ -surface calculations also suggest  $\frac{1}{3}[2\bar{1}\bar{1}3]$  and  $[0\bar{1}\bar{1}1]$  dislocations ( $\langle a+c \rangle$  or  $\langle c-b \rangle$  directions) in prismatic and pyramidal planes, which is also consistent with the experimental data. Phase A has a higher flow strength than olivine. When forming at depths from the dehydration of weak and highly anisotropic hydrated ultramafic rocks, phase A may not maintain the mechanical softening antigorite can provide. The seismic properties calculated for moderately deformed aggregates suggest that S-wave seismic anisotropy of phase A-bearing rocks is lower than hydrous subduction zone lithologies such as serpentinites and blueschists.

© 2015 The Authors. Published by Elsevier B.V. This is an open access article under the CC BY-NC-ND license (<http://creativecommons.org/licenses/by-nc-nd/4.0/>).

### 1. Introduction

Phase A ( $\text{Mg}_7\text{Si}_2\text{O}_8(\text{OH})_6$ ) is a dense hydrous magnesium silicate (DHMS) phase which forms mainly by destabilization of Mg-phylosilicates in hydrated lithologies, between 200 and 350 km depths in cold hydrous parts of the subducting slabs. Because of its chemical composition, phase A is the major water carrier at these depths and is viewed as a key phase for water transfer from the serpentine stability field down to the transition zone in cold environments (e.g. Poli and Schmidt, 1997). Subduction zone seismic velocities and anisotropies can be used

for mapping water-rich rocks in subduction zone. Phase A has a lower anisotropy than other hydrous phases in the mantle (Sanchez-Valle et al., 2006, 2008), therefore it is not expected to have a large contribution to seismic anisotropy within subduction zones (Mainprice and Ildefonse, 2009) unless it acquires a strong LPO during deformation. The contribution of phase A to anisotropy still needs to be assessed from deformation experiments, and could help inferring the “hydration state” of subducting slabs. Also, the sustainability at depth of shear zones formerly filled with Mg-phylosilicates, known to be extremely weak (Hilairot et al., 2007; Amiguet et al., 2012), may depend on rheological properties of phase A. These shear zones influence in turn the slab ability to deform upon sinking towards the transition zone.

Mussi et al. (2012) proposed a first study of the deformation mechanisms of phase A over a 400–700 °C temperature range at 11 GPa, using transmission electron microscopy (TEM) on

\* Corresponding author at: Université Lille 1, Unité Matériaux et Transformation, UMR CNRS 8207 – Bat C6, ENSCL, 59655 Villeneuve d'Ascq Cedex, France. Tel.: +33 320 434861.

E-mail address: [Karine.Gouriet@univ-lille1.fr](mailto:Karine.Gouriet@univ-lille1.fr) (K. Gouriet).

samples recovered after stress relaxation experiments. Here, we studied phase A deformation mechanisms and rheology using two independent approaches: High-pressure high-temperature (HP-HT) deformation experiments with *in situ* measurements using synchrotron X-ray diffraction (XRD), and computational methods based on the Peierls–Nabarro–Galerkin (PNG) model and generalized stacking faults ( $\gamma$ -surface) calculations. HP-HT experiments allow measuring rheological properties of polycrystals and LPO that result from the deformation mechanisms at play; they take into account the complexity of polycrystal deformation. PNG computations, by looking at the easiness of shear paths in the crystal structure, and at the fine structure of dislocation cores – hence their mobility – provide additional constraints on the geometry of slip, which determines the development of LPO.

Our results highlight the complementarity and limits of these two approaches. They are in global agreement with, and refine the conclusions from the TEM study by [Mussi et al. \(2012\)](#). Finally we discuss briefly the implications for the contribution of phase A to deformation and seismic velocities of hydrous regions in subducting slabs.

## 2. Experimental and computational methods

### 2.1. Experimental methods

Phase A polycrystals were deformed at high pressure and high temperature, with *in situ* measurements of flow strength and LPO. A proper analysis of the LPO, e.g. using viscoplastic self-consistent modeling helps to constrain the slip systems involved during deformation, assuming dislocation activity is causing the LPO. LPO measurements coupled with knowledge of the single crystal elasticity allow calculating seismic velocities for the polycrystals that can be directly compared to those observed in subduction zones.

#### 2.1.1. Synthesis and deformation experiments

The polycrystalline phase A samples were synthesized from oxide powders in stoichiometric proportions and free water in excess, in the 1500T multi-anvil press facility of the Institut National des Sciences de l'Univers (INSU) in Clermont-Ferrand, France. A 14 M multi-anvil assembly was used with 8 mm truncations on 32 mm-sided cubes. The pressure for all runs was 11 GPa, based on fixed-points calibrations. Temperatures were between 880 and 950 °C and run durations from 4 to 12 h. The recovered samples were loose grains, as a result of adding water in the capsules. They were analyzed at the INSU Raman spectroscopy facility at the ENS Lyon, France, and confirmed to be pure phase A. The samples were cold pressed before being loaded for deformation experiments.

The deformation experiments were carried out in the D-DIA large-volume press at 13-BM-D, GSE-CARS, at the Advanced Photon Source ([Wang et al., 2003](#)), with 3 mm truncation anvils and 5 mm edge cells. The samples were shortened in one deformation cycle only. Sample axial strains were measured using X-ray radiography over 8 s with a  $2 \times 3$  mm monochromatic beam. The strain is defined as  $\varepsilon = (l - l_0)/l_0$ ,  $l$  being the sample length and  $l_0$  the reference length taken at the beginning of the deformation (advance of differential rams).

Lattice strains and preferred orientations were recovered from 2-dimensional (2D) XRD patterns, collected over 300 s with an area detector (MAR165 CCD) and a monochromatic beam (wavelength  $\lambda = 0.2066$  Å) collimated to  $200 \times 200$   $\mu\text{m}$  by WC slits. Detector tilt and rotation relative to the incident beam were calibrated with a CeO<sub>2</sub> standard using Fit2D ([Hammersley et al., 1996](#)). The detector

spatial drift was systematically corrected by fitting the diffraction center during the data processing (Section 2.1.2).

Unfortunately the samples could not be recovered for further investigations such as scanning electron microscopy (SEM) and electron back-scattered diffraction (EBSD). Due to blowouts at the end of each deformation cycle the cells were pulverized. Therefore we rely only on the *in situ* data for samples preferred orientations. These have been shown to agree well with preferred orientations measured on post-mortem silicate samples using EBSD ([Bollinger et al., 2012](#)).

#### 2.1.2. Diffraction data processing

For a polycrystal under differential stress, departure of the powder diffraction pattern from ideal rings is a proxy for the differential stress supported (e.g. [Uchida et al., 1996](#)). This departure is referred to as “lattice strain”. The isotropic component of the stress, close to the confining pressure, can also be recovered (see e.g. [Hilaret et al. \(2012\)](#) and the [Supplementary material Fig. S1](#)). The analysis was carried out using the Multifit – Polydefix software available online at <http://merkel.zoneo.net/Multifit-Polydefix/> ([Merkel and Hilaret, 2015](#)).

Unit cell volumes were refined based on  $d$ -spacing  $d_p(hkil)$  of 4 diffraction lines ( $11\bar{2}0$ ,  $11\bar{2}1$ ,  $20\bar{2}2$ ,  $12\bar{3}2$ ). Confining pressures were calculated following a third-order finite strain equation of state by [Sanchez-Valle et al. \(2006, 2008\)](#).

Differential stresses  $t(hkil)$  were calculated for these planes from lattice strains  $Q(hkil)$  according to  $t(hkil) = 6Q(hkil)G(hkil)$ .  $G(hkil)$  are calculated from the single crystal elastic moduli of phase A ([Sanchez-Valle et al., 2008](#)). The temperature effect on the  $C_{ij}$ 's is not known. A decrease in  $C_{ij}$  of 6% similar to the one for olivine between ambient T and 580 °C, gives a 100 to 200 MPa difference in calculated  $t(hkil)$ , which is small compared to the observed stresses discussed in the following. In order to evaluate the flow strength, a “macroscopic” sample flow stress was extracted by averaging observed  $hkil$  reflections ([Suppl. Mat. Fig. S1](#)). This approach is biased by the availability of diffraction lines, and is used in many studies because no simple relationship exists for calculation of macroscopic stresses from powder diffraction data (e.g. [Hilaret et al., 2012](#) for a discussion).

The texture was refined with the E-WIMV algorithm, a modification of WIMV ([Matthies and Vinel, 1982](#)). We used the software MAUD ([Lutterotti et al., 2007](#)) with a procedure similar to that described by [Miyagi et al. \(2006\)](#). In the case of axial compression, the strain of the sample can be approximated as axially symmetric and textures can be fully represented with an inverse pole figure (IPF), showing the orientation distribution of the compression direction relative to the crystal coordinates. Pole densities are expressed in multiples of random distribution (mrd). For a random polycrystal, all orientations have a density of 1 mrd. In a single crystal, the mrd is equal to infinity for one orientation and 0 for the others. For hexagonal materials such as phase A, only one 12th of the hemisphere is needed to fully represent the orientation distribution function (ODF). Here we use a 6th of the hemisphere because this is the only option in MAUD. The diffraction patterns were divided in angular slices of 10°, which is therefore the lowest meaningful resolution for the ODF. We used a 15° resolution for the ODF. No smoothing filter was applied. Initially no sample symmetry was assumed during analysis in order to check if the axial symmetry could be observed in the experimental and reconstructed pole figures (e.g., [Miyagi et al., 2006](#)). Once this cylindrical symmetry was observed, a cylindrical geometry was imposed for the final fits. The [Fig. S2 in the Suppl. Mat.](#) compares the experimental data and the fit for the final texture of the run D1366. The goodness of the fits was assessed visually on these plots and from the Rw factors for the refinements in MAUD which were less than 4%, a satisfactory value.

## 2.2. Computational methods

First-principles calculations were used to obtain the structural parameters and elastic properties of phase A. Then, a two-step approach was used to investigate possible slip systems in phase A. First, we investigated the ease of shear in a number of dense planes of the structure by calculating so-called generalized stacking faults and  $\gamma$ -surfaces. This is an efficient numerical tool to look for easy shear paths in a given crystalline structure and to constrain potential slip systems. Secondly, based on this selection, we modeled dislocations, which are the agents of deformation responsible for the development of LPO. Easy slip systems in a given structure are those where dislocations are mobile and produce plastic strain. The fine structure of dislocation cores is a key parameter in determining their mobility. Namely, dislocations glide easily in the planes where their cores spread. In this study, we modeled core spreading using a so-called Peierls–Nabarro approach, which uses  $\gamma$ -surface as an input from the atomic scale.

### 2.2.1. Ground properties (*ab initio*) calculations

First-principles calculations have been performed based on the density functional theory (DFT) within the generalized gradient approximation (GGA) (Perdew and Wang, 1992). Calculations were performed using the VASP code (Kresse and Hafner, 1993, 1994; Kresse and Furthmüller, 1996a,b) and the all-electron projector augmented-wave (PAW) method (Blochl, 1994; Kresse and Joubert, 1999). The outmost core radii are 2.00 a.u. for Mg atoms, 1.9 a.u. for Si atoms, 1.52 a.u. for O and 1.1 a.u. for the H atoms. With the pseudo-potentials used in this work, 2s 0p states for Mg, 2s 2p states for Si and 2s 4p states for O are treated as valence states. All calculations have been performed using a single cut-off energy value of 400 eV for the plane wave expansion and a Monkhorst–Pack grid (Monkhorst and Pack, 1976) scheme was used for first Brillouin zone sampling.

Mg<sub>7</sub>Si<sub>2</sub>O<sub>8</sub>(OH)<sub>6</sub> was optimized (full relaxation of cell parameters and of atomic positions) using a 16 × 16 × 8 K-point mesh and the athermal elastic constant were determined from Hooke's Law:  $[\sigma] = [C][\epsilon]$ . For a hexagonal lattice there are five independent elastic constants, usually referred to as  $C_{11}(=C_{22})$ ,  $C_{12}$ ,  $C_{13}$ ,  $C_{33}$  and  $C_{44}(=C_{55})$  (Wallace, 1970) and the sixth elastic constant is given by  $C_{66} = (C_{11} - C_{12})/2$ . Then Hooke's Law is simplified:

$$\begin{pmatrix} \sigma_1 \\ \sigma_2 \\ \sigma_3 \\ \sigma_4 \\ \sigma_5 \\ \sigma_6 \end{pmatrix} = \begin{pmatrix} C_{11} & C_{12} & C_{13} & & & \\ C_{12} & C_{11} & C_{13} & & & \\ C_{13} & C_{13} & C_{33} & & & \\ & & & C_{44} & 0 & 0 \\ & & & 0 & C_{44} & 0 \\ & 0 & & 0 & 0 & C_{66} \end{pmatrix} \begin{pmatrix} \epsilon_1 \\ \epsilon_2 \\ \epsilon_3 \\ \epsilon_4 \\ \epsilon_5 \\ \epsilon_6 \end{pmatrix}$$

These quantities were estimated by applying (Cover et al., 2009) a set of strains  $\epsilon$  with the axis “3” taken along the  $c$  axis. The five configurations used to obtain the elastic constants at 10 GPa are given in Suppl. Mat. Table S1.

### 2.2.2. Generalized Stacking Fault energy calculations

Calculating a  $\gamma$ -surface for a given slip system requires a supercell with a geometry adapted to the shear plane and direction. We built supercells on a Cartesian reference frame defined by the normal of the stacking fault plane and by the shear direction. A vacuum buffer is added in the direction normal to the slip plane to avoid interaction between repeated stacking faults resulting from the use of periodic boundary conditions in 3D.  $\gamma$ -Surfaces are computed as follows. Atoms on surfaces along the direction normal to the glide plane are imposed at fixed positions and all other atoms are allowed to relax in the direction perpendicular to the shear plane in order to minimize energy of the  $\gamma$ -surface. Further details

of the supercell construction and relaxation conditions can be found elsewhere (Durinck et al., 2005). Thus, for all the  $\gamma$ -surface calculations, three distinct supercells were used (Suppl. Mat. Fig. S3). The number of atoms per supercell is 58 for the basal plane and 116 for the both prismatic planes. The  $\gamma$ -surface excess energies  $\gamma$  are finally calculated by imposing a given shear displacement value to the upper part of the supercell.

### 2.2.3. The Peierls–Nabarro–Galerkin model

In the PNG model, the dislocation core structure naturally emerges from the minimizing of an elastic energy and of an interplanar potential. Displacement fields are represented by an element-free Galerkin method. The non-linear behavior is ensured by a displacement jump along potential glide planes of the structure associated with an extra cost in energy attributed to the interplanar potential. The latter is a function of the  $\gamma$ -surface energies (to be defined in the next section) from which the linear elastic part has been subtracted. In doing so, the method allows to take into account for several potential glide planes simultaneously and thus to calculate complex (possibly three-dimensional) dislocation cores. Once the nodal mesh supporting  $\gamma$ -surface energies is defined, a discrete Volterra dislocation is introduced into the volume. Boundary conditions, consistent with a dislocation in an infinite medium, are used by imposing a convolution of an elementary elastic solution with the dislocation density (see Pillon and Denoual, 2009 for implementation details). The equilibrium of displacement jump field  $f$  and the Burgers vector density  $\rho$ , as defined as the derivative of  $f$  by the position coordinates, are finally determined through a viscous relaxation scheme. Extended details of the PNG method are available in Denoual (2007), Pillon et al. (2006, 2007) or Pillon and Denoual (2009). The nodal meshes used in this study are built with respect to the  $P6_3$  symmetry of Mg<sub>7</sub>Si<sub>2</sub>O<sub>8</sub>(OH)<sub>6</sub> (Horiuchi et al., 1979). Three different meshes are thus used here and the dislocation line is along the  $z$  direction.

For each dislocation, we select the first low ( $hkl$ ) crystallographic plane to control the periodic variation of the dislocation core energy as a function of its position. For all calculations, meshes dimensions were equivalent to 30 phase A unit cells with a nodal resolution of 16 nodes per Burgers vector. Accordingly to Denoual (2007), we checked that increasing mesh dimensions or nodes number did not influence the results. First calculations corresponded to the relaxation of the dislocation core structure. In a second step, we evaluated the Peierls stress corresponding to the relaxed core. At this stage, a homogeneous deformation was progressively applied at a velocity that allowed quasi-static equilibrium so as to induce an applied shear stress on a unique given glide plane. During this loading stage, noticeable evolution of the core structure may occur prior to a strong relaxation of the measured stress. Such relaxation of the measured stress is associated with a rapid evolution of the dislocation core structure followed by a displacement of one (or more) Burgers vector(s). In the following, the Peierls stress will be associated with this ultimate macroscopic stress (Metsue et al., 2010).

## 3. Results

### 3.1. Experimental and VPSC results

The lattice strains vs. bulk strain curves for the three experimental runs are shown in Fig. 1. The flow stresses depend on temperature (Table S2), varying from 3.2–3.3 at 400 °C to 2.5 GPa at 580 °C. Macroscopic stress vs. strain curves are also reported Fig. S1. Because strain rates were slightly different at the two temperatures and in the absence of data for the thermal dependence of

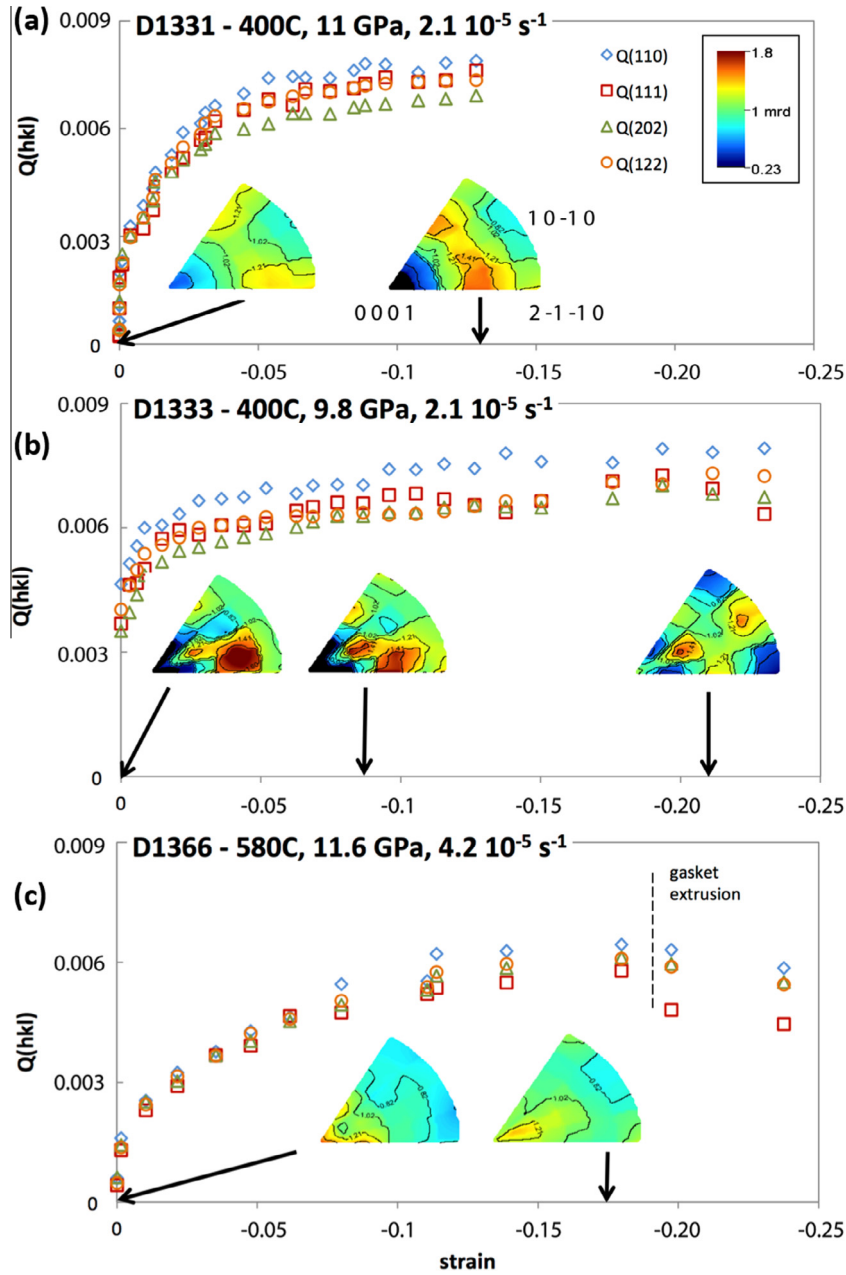


**Fig. 1.** Experimental results: lattice strains (proxy for the differential stress) – bulk strain curves and textures refined from *in situ* XRD (inverse pole figures for the maximum compressive axis). We attribute the difference in texture between 400 °C runs and 580 °C run to a change in slip systems contributions on the basis of VPSC modeling (Fig. 2). The starting texture for run D1333 shows a strong maximum due to spottiness on the diffraction, which is an unstable orientation since this maximum disappears with increasing strain. (Color online.)

phase A elastic moduli, temperature and strain rate dependence could not be quantified.

The preferred orientations refined at the beginning and the end of deformation, are also shown in Fig. 1. All samples, after compression, and before starting deformation at high temperature are slightly to moderately textured. Because of a large (compared to the beam size) grain size at the beginning of run D1333, the XRD pattern is spotty, and the starting texture shows a pronounced maximum slightly deviated from  $\langle c+a \rangle = \frac{1}{3}[2\bar{1}\bar{1}3]$ . Therefore, we did not try to model these intermediate-strain textures and do not use them for interpretation in terms of slip systems. The two runs at 400 °C have different starting textures. At 10% strain the LPO still shows the starting maxima, while intensities increased

in the  $\langle c+b \rangle = [10\bar{1}1]$  orientation and decreased in the  $\frac{1}{3}[2\bar{1}\bar{1}0]$  orientation. In D1333 where bulk strain reached 20%, the initial maxima vanished while maxima up to 1.6 mrd at  $[10\bar{1}1]$  and at  $[10\bar{1}0]$  developed, together with strong minima (0.23 mrd) at  $\frac{1}{3}[2\bar{1}\bar{1}0]$  (Fig. 1b). Note that in run D1331, the maxima around  $\frac{1}{3}[2\bar{1}\bar{1}0]$  decrease with increasing strain, therefore we consider this texture as consistent with the ones obtained in D1333. In summary at 400 °C, the stable maxima to develop with strain are at  $[10\bar{1}1]$  and  $[10\bar{1}0]$ .

The run at 580 °C has a different starting texture with a weak maximum towards  $[0001]$  (Fig. 1c) and a girdle with minimum lower than 0.82 mrd from  $\frac{1}{3}[2\bar{1}\bar{1}0]$  to  $[10\bar{1}0]$ . At 18% bulk strain,

the maximum at [0001] increases above 1.21 mrd and slightly deviates from [0001] while the girdle fades away, with a minimum of 0.76 mrd at  $[10\bar{1}0]$ .

In order to interpret the differences in LPO in term of activated slip systems, we used viscoplastic self-consistent (VPSC) modeling (Lebensohn and Tomé, 1993). This model uses the principle of inclusion formalized by Eshelby (1957) in order to analyze the viscoplastic interaction between a grain and a matrix constituted from all other grains. The deformation is prescribed and imposed incrementally on a set of grains described by their orientations. Slip systems to be activated are proposed each with a viscoplastic law. The LPO evolution throughout deformation can be followed. The results of six simulations are shown in Fig. 2 and their parameters are summarized in Table 1. The experimental starting LPO of the corresponding runs were used as starting points for the simulations (Table 1).

Simulations A and E (Fig. 2) best represent the final textures of the data at 400 °C (D1331 and D1333) and 580 °C (D1366), respectively. Although the final IPF in D1331 looks more similar to model C than model A, model C is not consistent with the whole history of run D1331 which show that intensity at  $\frac{1}{3}[2\bar{1}\bar{1}0]$  decreases with increasing bulk strain.

In A, most similar to the lowest temperature experiments, the  $\langle\bar{1}100\rangle\{2\bar{1}\bar{1}0\}$  slip system contributes to more than 50% and the pyramidal and basal contribution are respectively around 26 and 18%. The experimental texture at the highest temperature (Fig. 1) can be explained by simulation E, where the basal mode contributes more than 70%, and a contribution at 27% from a prismatic mode different than the lowest temperature one.

### 3.2. Computational results

The LPO and VPSC models do not always lead to a unique interpretation of the slip systems. For instance, Burgers vectors  $\langle a \rangle$  (i.e. with  $\frac{1}{3}[2\bar{1}\bar{1}0]$  direction) and  $\langle b \rangle$  (i.e. with  $[01\bar{1}0]$  direction) in the basal plane will not be distinguished by an analysis using VPSC, because a displacement along  $\langle b \rangle$  can be produced by a combination of displacements along  $\langle a \rangle$ . Thus we complemented our study by calculations aimed at constraining the easiest slip systems in phase A.

In this work, the structural optimization was first performed for the perfect  $\text{Mg}_7\text{Si}_2\text{O}_8(\text{OH})_6$  crystal structure at 10 GPa. The calculated lattice parameters and elastic constants are shown in Table 2. Our results are in good agreement with experimental and other theoretical values. Only  $C_{12}$  is softer than Sanchez-Valle et al. (2008). We first present the results of  $\gamma$ -surfaces calculations before those on dislocation core modeling.

#### 3.2.1. $\gamma$ -Surface results

Experimental results highlight the potential contribution of several planes for plastic slip: the basal plane, the prismatic planes (of both  $\{01\bar{1}0\}$  and  $\{2\bar{1}10\}$  types) and the type I pyramidal plane. We computed  $\gamma$ -surfaces for the basal and both prismatic planes. The pyramidal plane reaches the limit of *ab initio* calculations (time and number of atoms) and will not be considered here.

The  $\gamma$ -surfaces of the basal plane, and of the  $(01\bar{1}0)$  and  $(2\bar{1}10)$  prismatic planes are shown in Fig. 3. Local minima of the  $\gamma$ -surfaces correspond to potential stable stacking faults in the structure which can possibly lead to dissociation of dislocations

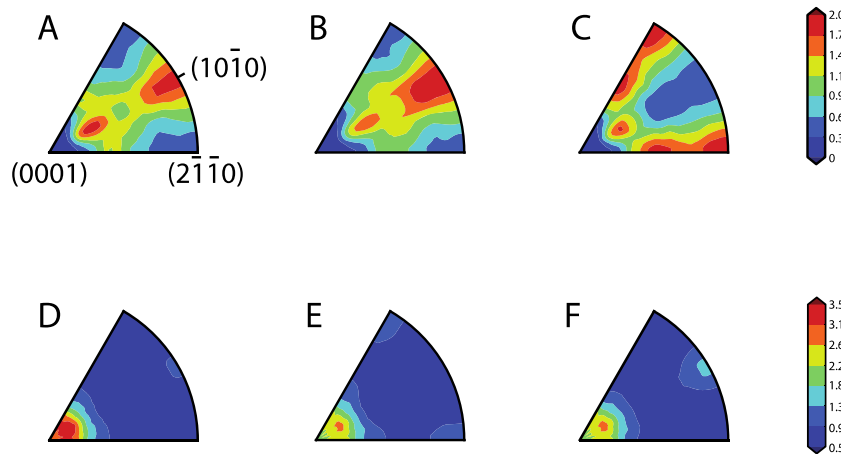


**Fig. 2.** Inverse pole figures for the maximum compressive axis resulting from the VPSC models, with run parameters Table 1. (A) and (E) best reproduce the experimental textures at ca. 400 °C and ca. 580 °C respectively (cf. Section 3.1). (Color online.)

**Table 1**

VPSC run parameters and resulting activities for the slip systems (normalized to 1 for the total activity of all systems).

Model	Starting texture	Slip modes CRSS ( $\tau_0$ , GPa) (input)					Activities of slip modes at 15% strain (output, normalized to 1)				
		$\langle 2110 \rangle$ $\{0001\}$ Basal $\langle a \rangle$	$\langle 2110 \rangle$ $\{0\bar{1}10\}$ Prismatic 1st order $\langle a \rangle$	$\langle 1100 \rangle$ $\{2110\}$ Prismatic 2nd order $\langle 1100 \rangle$ partials	$\langle 2113 \rangle$ $\{11\bar{2}1\}$ Pyramidal $\langle c+a \rangle$ $\{111\}$	$\langle 2113 \rangle$ $\{0001\}$ Basal $\langle a \rangle$	$\langle 2110 \rangle$ $\{0\bar{1}10\}$ Prismatic 1st order $\langle a \rangle$	$\langle 1100 \rangle$ $\{2110\}$ Prismatic 2nd order, $\langle 1100 \rangle$ partials	$\langle 2113 \rangle$ $\{11\bar{2}1\}$ Pyramidal $\langle c+a \rangle$ $\{111\}$		
A	D1333	2		1	2	0.23		0.61	0.16		
B	D1333	20		1	2	0		0.66	0.34		
C	D1333	2	1		2	0.18	0.56		0.26		
D	D1366	1	10		10	0.98	0.007		0.013		
E	D1366	1	2		4	0.73	0.20		0.07		
F	D1366	1		2	4	0.73		0.20	0.07		

**Table 2**  
Lattice parameters in Angstroms and elastic constants in GPa.

	<i>Ab initio</i>	Experimental
$a$	7.6196 <sup>a</sup>	7.8563 <sup>b</sup>
$c$	9.3481 <sup>a</sup>	9.5642 <sup>b</sup>
$C_{11}$	245	248 <sup>c</sup>
$C_{33}$	295	296 <sup>c</sup>
$C_{55}$	84	86 <sup>c</sup>
$C_{12}$	97	129 <sup>c</sup>
$C_{13}$	93	93 <sup>c</sup>

<sup>a</sup> Relaxed parameters obtained after extrapolation from Crichton and Ross (2002).

<sup>b</sup> Values used in the experiments from Kagi et al., 2000.

<sup>c</sup> Extrapolation of Sanchez-Valle et al., 2008.

into partials. In the basal plane (see Fig. 3a), three stable stacking faults are observed:  $\gamma_0 = 2.11 \text{ J/m}^2$ ,  $\gamma_1 = 2.72 \text{ J/m}^2$  at  $\frac{1}{21}\langle 5\bar{1}40 \rangle$  and  $\gamma_2 = 3.42 \text{ J/m}^2$  at  $\frac{1}{3}\langle 01\bar{1}0 \rangle$ . As a consequence, we expect  $\frac{1}{3}[2\bar{1}\bar{1}0]$  ( $\langle a \rangle$  in the following) and  $[01\bar{1}0]$  ( $\langle b \rangle$  in the following) dislocations to be dissociated in the basal plane with a dissociation path exploring these three stable stacking faults. In prismatic planes, a stable stacking fault is observed close to  $\frac{1}{2}[0001]$  in  $(01\bar{1}0)$  ( $\gamma_1^1$  in Fig. 3b) and a broad plateau is observed along the  $[0001]$  ( $\langle c \rangle$  in the following) direction in  $(2\bar{1}\bar{1}0)$  ( $A_{II}C_{II}$ ; Fig. 3c and e). In prismatic planes, the most pronounced local minima are not along  $\langle c \rangle$ , but along the diagonal directions i.e. along  $\frac{1}{3}[2\bar{1}\bar{1}3]$  (or  $\langle c+a \rangle$  along  $A_{II}D_I$ , see Fig. 3b and d) in  $(01\bar{1}0)$  and along  $[0\bar{1}11]$  (or  $\langle c-b \rangle$  along  $B_{II}C_{II}$  see Fig. 3c and e) in  $(2\bar{1}\bar{1}0)$  respectively.

### 3.2.2. Dislocation core structures

To further constrain the easiness of slip in those planes, we calculate the dislocation core structures to assess lattice friction from the tendency of core spreading in a given plane. Dislocation core structures are calculated with the PNG model using, as an input,  $\gamma$ -surfaces and also the elasticity tensor calculated *ab initio* with VASP. For each dislocation, we build the PNG model by introducing several planes which contain the line direction of the dislocation. The behavior of each plane is governed by the  $\gamma$ -surfaces corresponding to the planes (among  $(0001)$ ,  $(01\bar{1}0)$  and  $(2\bar{1}\bar{1}0)$ ). The rest of the cell behaves elastically. For details of each cell, see the Supplementary material Fig. S4 and Table S3. To represent the core structure, we focus on the disregistry  $f$  (parallel to the Burgers vector) by plotting the node disregistries as a function of the distance from the core in both planes. The tendency for core spreading is indicated by a shoulder on the disregistry curve (or by presence of more than one peak on the associated Burgers vector density  $\rho(x) = df(x)/dx$ ), and in particular for the edge dislocation which presents the larger width. As such a feature may indicate a tendency for dissociation, we performed a smooth fitting of the disregistry functions using a sum of *atan* functions (Eq. (1)), we rely on the canonical analytical solution (i.e.  $i=0$  and  $x_i=0$  in Eq. (1)) of Peierls (Peierls, 1940).

$$f(x) = \frac{b}{2} + \frac{b}{\pi} \sum_i \alpha_i \text{atan} \left( \frac{x - x_i}{\zeta_i} \right) \quad (1)$$

The Peierls stresses ( $\sigma_p$ ) for the each slip systems investigated here have been evaluated by shearing the PNG nodal mesh. All the parameters describing the calculated relaxed cores (as well as the Peierls stresses) that we will describe now are summarized in Table 3.

In this work, we first focus on screw dislocations. Having their Burgers vector parallel to their line directions, screw dislocations are not ascribed to glide in a specific plane. However their core structure may induce some strong constraints. Screw dislocations

usually glide in the planes where they exhibit core spreading. This is a strong constraint on glide plane selections.

In a hexagonal structure,  $\langle a \rangle$  and  $\langle b \rangle$  dislocations can potentially glide in the basal plane, in prismatic or in pyramidal planes. Here by modeling screw dislocations with the PNG model with  $\gamma$ -surfaces corresponding to the  $(0001)$ ,  $(01\bar{1}0)$  and  $(2\bar{1}\bar{1}0)$  planes we assess the tendency of these dislocations to glide in the basal or in prismatic planes. We show that these dislocations spread widely in the basal plane only. Core spreading even leads to dissociation into several partials (Fig. 4a and Suppl. Mat. Fig. S5 resp) with a core width of 10 Å for  $\langle a \rangle$  and 35 Å for  $\langle b \rangle$ . This represents respectively 1.5 and 5 times the  $a$  lattice parameter in the basal plane (see Suppl. Mat. Figs. S6 and S7). The dissociation path for the  $\langle a \rangle(0001)$  screw dislocation is plotted on the  $\gamma$ -surface in Fig. 4b. To further assess the tendency of  $\langle a \rangle$  and  $\langle b \rangle$  dislocations to glide preferentially in the basal plane, we have calculated the core structure of the edge dislocations. Edge dislocations have to be considered independently in the basal plane and in their prismatic planes. We find that both edge  $\langle a \rangle$  and  $\langle b \rangle$  dislocations spread and dissociate in the basal plane (see Supplementary material Figs. S6 and S7) with dissociation widths similar to screws. In prismatic planes, we find  $\langle a \rangle$  and  $\langle b \rangle$  edge dislocations to exhibit a narrow core which suggest a high lattice friction. Indeed this is what is found when the nodal mesh is sheared to find the Peierls stresses, see Table 3. Altogether, these results show a marked tendency of  $\langle a \rangle$  and  $\langle b \rangle$  dislocations to glide in the basal plane compared with their respective prismatic planes.

In prismatic planes we can also calculate the core structure of  $\langle c \rangle$  dislocations. Again, we start by the calculation of the core structure of screw dislocations. However, a unique core structure cannot be found for  $\langle c \rangle$  dislocations. When it is introduced in the  $(01\bar{1}0)$  prismatic plane, the  $\langle c \rangle$  screw dislocation spreads and dissociate into two collinear components with a wide spreading of 10 Å (i.e. approximately the lattice repeat along  $c$ ; see Suppl. Mat. Fig. S8). However, when it is introduced in the  $(2\bar{1}\bar{1}0)$  prismatic plane, the  $\langle c \rangle$  screw dislocation also dissociates into three partials with mixed components and a wide spreading of 14 Å (i.e. approximately 1.5 times the  $c$  lattice parameter; see Suppl. Mat. Fig. S8). The edge components exhibit, in each prismatic plane, core profiles very similar to screws. Hence the PNG model fails to find a unique stable core structure for  $\langle c \rangle$  screw dislocations.

## 4. Discussion

### 4.1. Deformation mechanisms in phase A, from micro to macro?

Here, we integrate the results from computations, experiments and TEM (Mussi et al., 2012) for each type of glide planes: basal, prismatic and pyramidal, successively.

Given the layered configuration of phase A lattice, the basal plane exhibits the lowest values of the stacking fault energies (Fig. 3a) and is expected to be an easy glide plane. Indications from computations, experiments (this study), and TEM (Mussi et al., 2012) are all consistent and characterize completely glide in this plane.

In the basal plane, two Burgers vectors are considered for the computations:  $\langle a \rangle$ , which is the shortest lattice vector in this structure, and  $\langle b \rangle$ . The dislocations with the  $\langle a \rangle$  Burgers vector show a core dissociated into three partials in the basal plane (Fig. 4a):

$$\langle a \rangle \rightarrow \frac{1}{21}\langle 5\bar{4}\bar{1}0 \rangle + \frac{1}{21}\langle 4150 \rangle + \frac{1}{21}\langle 5\bar{4}\bar{1}0 \rangle \quad (2)$$

The dislocations with  $\langle b \rangle$  show a more complex dissociation involving six partials (Suppl. Fig. S5):

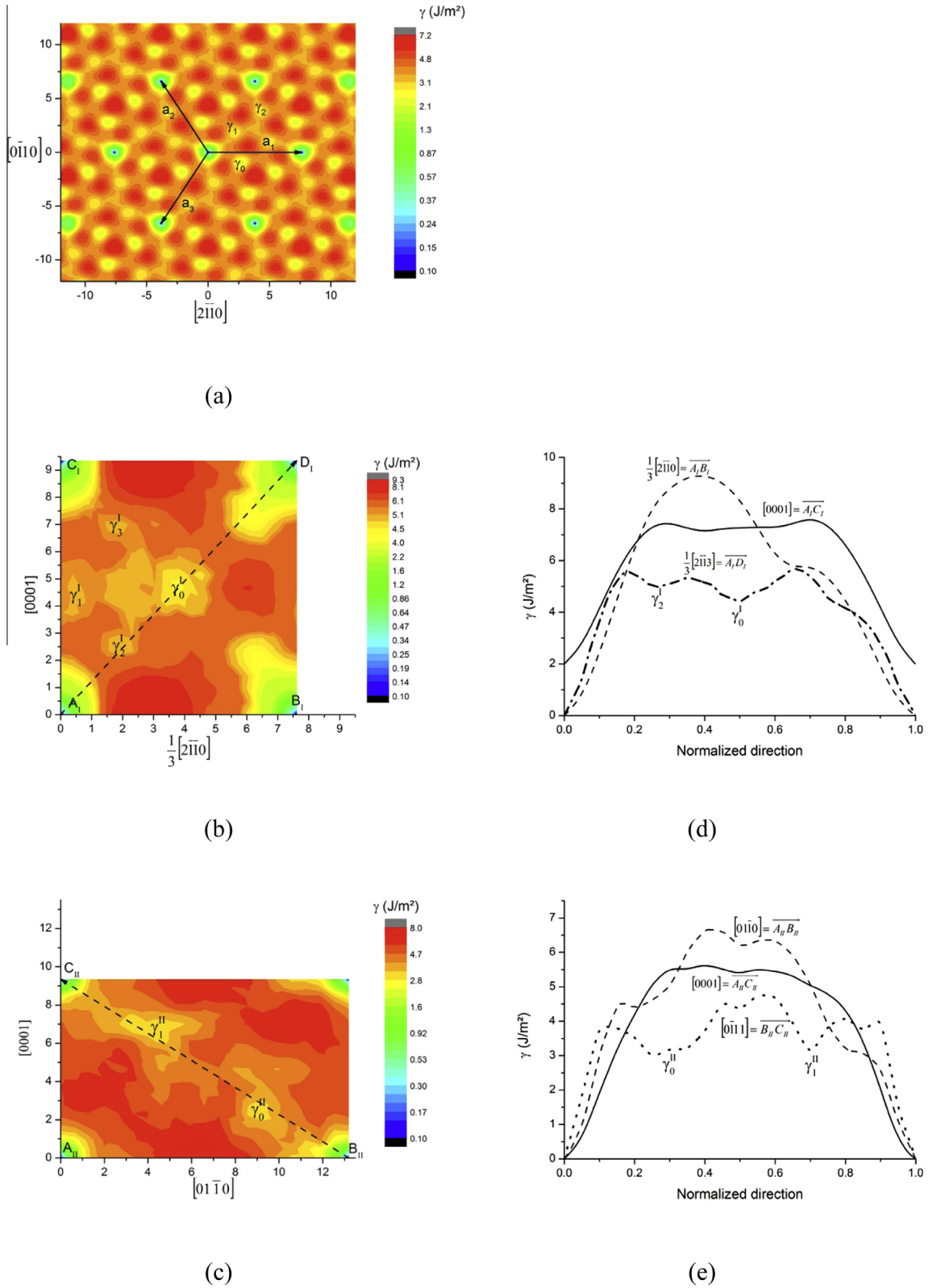


**Fig. 3.**  $\gamma$ -Surfaces (in  $\text{J m}^{-2}$ ) (a) of (0001) plane. The hexagonal base ( $a_1, a_2, a_3$ ) is represented,  $\gamma_0, \gamma_1$  and  $\gamma_2$  are the three stable stacking faults. (b) Of (01  $\bar{1}$  0) plane ( $\gamma_0^I, \gamma_1^I$  and  $\gamma_2^I$  are the three stable stacking fault) and (c) of (2  $\bar{1}$   $\bar{1}$  0) plane ( $\gamma_0^{II}$  and  $\gamma_1^{II}$  are the two stable stacking faults). (d)  $\gamma$ -Lines along  $\frac{1}{3}[2\bar{1}\bar{1}0], \frac{1}{3}[2\bar{1}\bar{1}3]$  and [0001] in (01  $\bar{1}$  0) plane as a function of normalized direction (vector/norm), for clarity, the [0001] curve is shifted vertically, and (e)  $\gamma$ -lines along [01  $\bar{1}$  0], [0  $\bar{1}$  1 1] and [0001] in (2  $\bar{1}$   $\bar{1}$  0) plane as a function of normalized direction (vector/norm). (Color online.)

$$\begin{aligned}
 (b) = & \frac{1}{21} \langle \bar{1}540 \rangle + \frac{1}{21} \langle \bar{1}540 \rangle + \frac{1}{21} \langle 41\bar{5}0 \rangle + \frac{1}{21} \langle 2\bar{3}\bar{1}0 \rangle \\
 & + \frac{1}{21} \langle 12\bar{3}0 \rangle + \frac{1}{21} \langle \bar{1}540 \rangle
 \end{aligned} \quad (3)$$

We note that in Eq. (3), the last two partials form the partial usually expected in basal plane for hexagonal materials:  $\frac{1}{3}b = \frac{1}{3}[01\bar{1}0]$ . Dislocations with the  $\langle a \rangle$  Burgers vector have the

**Table 3**

Summary of dislocation core parameters controlling the spreading in the corresponding plane and Peierls stresses  $\sigma_p$  (in GPa). Nb is the number of partials of the dislocation (NS: no spreading in this plane, 1: no dissociation).  $\Delta_m$  and  $\Delta_{Sum}$  (in Angstroms) are the mean partials separation distance and the total core respectively. S corresponds to the screw character, and E the edge character. NC indicates when the Peierls stress is not computed.

Plane	Char.	Nb	$\Delta_m$	$\Delta_{Sum}$	$\sigma_p$
$\frac{1}{3}[2\bar{1}\bar{1}0](0001)$	S	3	3.8	7.7	0.81
$\frac{1}{3}[2\bar{1}\bar{1}0](0001)$	E	3	3.7	7.5	1.94
$\frac{1}{3}[2\bar{1}\bar{1}0](01\bar{1}0)$	S	NS	–	–	NC
$\frac{1}{3}[2\bar{1}\bar{1}0](01\bar{1}0)$	E	1	–	–	4.9
$[01\bar{1}0](0001)$	S	6	4.4	26.5	1.47
$[01\bar{1}0](0001)$	E	6	6.8	34.0	2.6
$[01\bar{1}0](2\bar{1}\bar{1}0)$	S	NS	–	–	NC
$[01\bar{1}0](2\bar{1}\bar{1}0)$	E	1	–	–	7.3
$[0001](01\bar{1}0)$	S	2	6.2	6.2	NC
$[0001](01\bar{1}0)$	E	2	8.4	8.4	NC
$[0001](2\bar{1}\bar{1}0)$	S	3	4.5	9.0	NC
$[0001](2\bar{1}\bar{1}0)$	E	3	5.8	11.5	NC

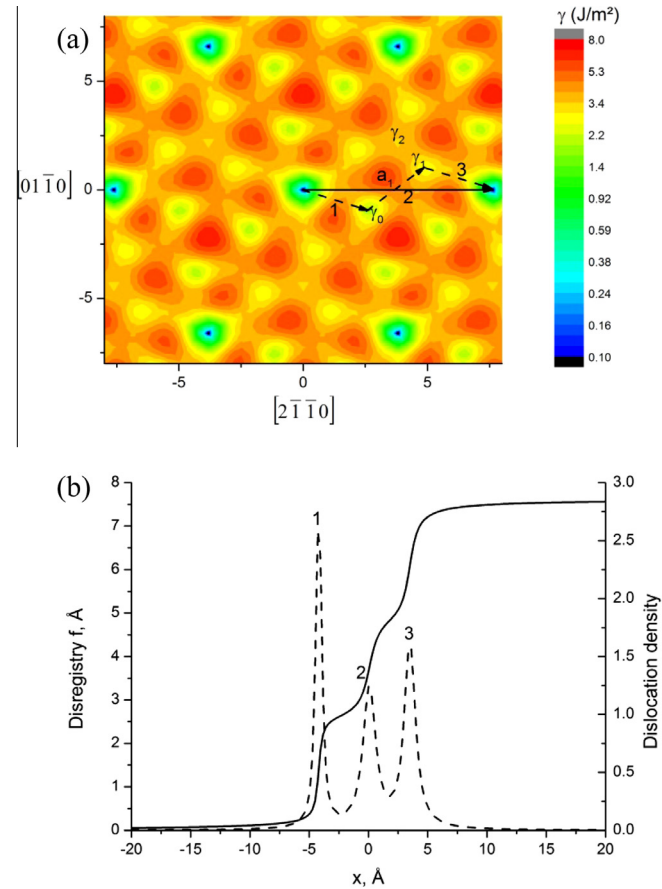


**Fig. 4.** (a) Core structure of  $\frac{1}{3}[2\bar{1}\bar{1}0]$  screw dislocation. Disregistry function  $f(x)$  and associated Burgers vector density  $\rho = df(x)/dx$  (dotted line) are plotted in (0001) plane. The number  $i$  corresponds to the  $i$ th partial in (b). (b)  $\gamma$ -Surfaces (in  $\text{J m}^{-2}$ ) of (0001) plane.  $\gamma_0$ ,  $\gamma_1$  and  $\gamma_2$  are the three stable stacking faults. The dash arrows represent the dissociation path of the dislocation with  $a_1$  as the Burgers vector and the number  $i$  corresponds to the  $i$ th partial. 1 and 3 correspond to  $\frac{1}{3}[5\bar{4}\bar{1}0]$  and 2 to  $\frac{1}{3}[4\bar{1}50]$ . (Color online.)

smallest Peierls stress (0.81 GPa for the screw and 1.9 GPa for the edge) while those with  $\langle b \rangle$  Burgers vector have larger, albeit still relatively low, values for the Peierls stress (1.5 GPa for screw and 2.6 GPa for edge).

Our results compare well with TEM observations by [Mussi et al. \(2012\)](#) who report significant dislocation activity in the basal plane. From the computations, glide in the basal plane is easy (large dissociation of dislocations resulting in a low lattice friction) compared to glide in prismatic planes ([Table 3](#)). VPSC simulations give consistent indications ([Table 1](#)): glide on the basal plane is required in all cases in order to reproduce the experimental textures, and contributes most to the deformation at the highest temperatures. Also, the dislocations with  $\langle a \rangle$  Burgers vectors observed in the basal plane by [Mussi et al. \(2012\)](#) appear as perfect ones. The equilibrium distances we compute between each partial of both  $\langle a \rangle$  and  $\langle b \rangle$  dislocations are indeed lower than 13 Å ([Fig. 4b](#) and [Suppl. Fig. S7](#)), meaning these individual partial dislocations cannot be resolved by TEM (best resolution in weak-beam dark-field is of the order of a few nanometers). Finally [Mussi et al. \(2012\)](#) observed in the basal plane a typical partial  $\frac{1}{3}[01\bar{1}0]$ . Our calculations indeed suggest a dissociation of  $\langle b \rangle$  dislocations which involve this component  $\frac{1}{3}[01\bar{1}0]$ .

Possible prismatic planes for glide are  $(01\bar{1}0)$  and  $(2\bar{1}\bar{1}0)$ , with  $\langle a \rangle$ ,  $\langle b \rangle$  or  $\langle c \rangle$  type Burgers vectors. VPSC modeling of the experimental data requires the  $\langle b \rangle\{2\bar{1}\bar{1}0\}$  slip system at low T, and the  $\langle a \rangle\{01\bar{1}0\}$  slip system at high T. From computations, a strong tendency for dissociation and core spreading is observed for screw dislocations in the basal plane. Edge dislocations face high lattice friction: the Peierls stress is 4.9 GPa for edge  $\langle a \rangle\{01\bar{1}0\}$  and 7.3 GPa for edge  $\langle b \rangle\{2\bar{1}\bar{1}0\}$ . Thus both slip systems appear much less favorable than  $\langle a \rangle\{0001\}$  and  $\langle b \rangle\{0001\}$ . Experimentally, although this difference is less marked, prismatic glide contribution diminishes at high T at the expense of basal glide.

Both  $(01\bar{1}0)$  and  $(2\bar{1}\bar{1}0)$  prismatic planes contain  $\langle c \rangle$  which is the longest lattice parameter (9.34 Å). PNG calculations show that  $\langle c \rangle$  screw dislocations may dissociate in both prismatic planes. PNG calculations appear unable to determine a unique stable configuration of the  $\langle c \rangle$  core structure, because of the existence of two possible dissociations in prismatic planes. An atomistic calculation of these  $\langle c \rangle$  dislocations appears necessary, should we have to determine their actual core structure. Such calculation demand an extremely large number of atoms, is very time intensive, and does not seem worth the computational effort: so far, no microscopic evidence for  $\langle c \rangle$  dislocations has been reported ([Mussi et al., 2012](#)), and such dislocations are not required to explain the experimental data.

In the present study, we could not model dislocations with  $\langle c+a \rangle$  or  $\langle c-b \rangle$  Burgers vectors. However, the observation of prismatic  $\gamma$ -surfaces leads to some hypotheses. In those planes, we observe that the most stable stacking faults are not along the  $\langle c \rangle$  direction, but along the  $\langle c+a \rangle$  and  $\langle c-b \rangle$  directions ([Fig. 3b](#) and [c](#)). Putative dislocations with these Burgers vector may well exhibit dissociation in prismatic planes and could provide an easier deformation mechanism than  $\langle c \rangle$  glide.

Finally, computing the pyramidal planes  $\gamma$ -surfaces is again too demanding. The  $\langle c+a \rangle\{11\bar{2}1\}$  slip system is however necessary in VPSC simulations to reproduce the experimental texture (model E, [Table 1](#)). TEM observations are consistent with the VPSC results: [Mussi et al. \(2012\)](#) also observed these type I pyramidal planes:  $(11\bar{2}1)$  and  $(11\bar{2}\bar{1})$ .

In summary, basal glide is easy and ubiquitous, necessary at both high and low temperatures, and is corroborated by computations. Prismatic glide operates along different directions,  $\langle a \rangle$  or  $\langle b \rangle$ , depending on T, but not along  $\langle c \rangle$ . Pyramidal  $\langle c+a \rangle$  glide significantly contributes to deformation at low temperature. Plastic relaxation along  $\langle c \rangle$  is likely to be provided by  $\langle c+a \rangle$  dislocations.

#### 4.2. Geophysical implications

Phase A is expected to form in cold descending slabs, as one of the products of serpentine dehydration (e.g. Komabayashi et al., 2005). Depending on the bulk composition and hydration of the parent serpentinized peridotite, phase A will constitute between 19% and 46% of a hydrated harzburgite (Sanchez-Valle et al., 2008; Hacker et al., 2003) with orthopyroxene as a major component along with less abundant olivine. The flow stress around 12% strain we measured on phase A is higher than that of olivine recalculated from its experimental flow laws, under the same pressure, temperature and strain rates (Table S2). Therefore within a typical aggregate composed of pyroxenes, olivine and phase A, phase A could be the stiffest phase. Phase A precursor, the serpentine variety antigorite, is weaker mechanically than olivine and pyroxene, and acts as a “strain localizing” phase within serpentinized peridotites. After serpentine dehydration, we suspect phase A will not play this strain localizing role because the strength contrasts between the components will be low. This would need to be confirmed with actual multiphase deformation experiments and experiments under larger strains.

The most significant anisotropy for phase A single crystals is the shear wave velocity anisotropy, about 20%, which is constant up to 11 GPa confining pressure (Sanchez-Valle et al., 2008). In spite of this significant anisotropy, phase A is one of the less anisotropic crystals among the hydrous phases in the mantle (Mainprice and Ildfonse, 2009) for  $V_p$  and  $V_s$ . In order to evaluate the contribution of phase A to shear wave velocity anisotropy within subduction zones, we calculated the seismic velocities for a pure phase A polycrystal with an experimental texture such as the one obtained at 580 °C (Fig. 5a) using the MTEX and MSAT packages (Bachmann et al., 2010; Walker and Wookey, 2012). The texture at 580 °C was used as it is relevant to cold subduction zones, while the

low T experiments are out of natural temperature ranges and have not been considered here. We used the  $C_{ij}$  and density at ambient pressure and temperature. Although the temperature dependence of the  $C_{ij}$  is unknown, increasing temperature is expected to decrease seismic velocities whereas increasing pressure has the opposite effect. According to Sanchez-Valle et al. (2008) pressure will only shift the values for seismic velocities, therefore first order anisotropic features should remain similar.

The experimentally deformed aggregate has P and S wave velocities close to the ones for hydrous eclogites, within the higher range of calculated values for blueschists and the lower range of those for peridotites (e.g. Bezacier et al., 2010). Therefore a phase A-rich lithology with this texture will be indistinguishable from the surrounding peridotites and eclogites on the basis of  $V_p$  and  $V_s$  values. The P wave velocity anisotropy is 2.4%, and the maximum S-wave velocity anisotropy  $AV_s$  is 3.29%. The maximum splitting occurs in the plane perpendicular to the compression axis with the fast wave polarized within a plane parallel to the compression axis. The minimum splitting is observed for propagation along the compression axis.

As commonly found in D-DIA experiments, the experimental texture is weak and likely cannot represent highly strained regions. In order to evaluate the effect of strain, we also calculated the seismic velocities for a hypothetical polycrystal from a VPSC simulation to 50% strain (Fig. 5b). We used the same deformation geometry, slip systems and CRSS as in model E, which reproduces the experimental texture at 580 °C. This phase A aggregate deformed to 50% bulk strain has a P-wave velocity anisotropy of 4.1% and a maximum S-wave velocity anisotropy of 5.5%. Such a S-wave velocity anisotropy is significant when considering the moderate amount of bulk strain involved. Olivine aggregates deformed in simple shear up to much larger strains by Ohuchi et al. (2011), for instance, do show S-wave anisotropies of about 5.5% at mantle wedge conditions. This S-wave anisotropy is also

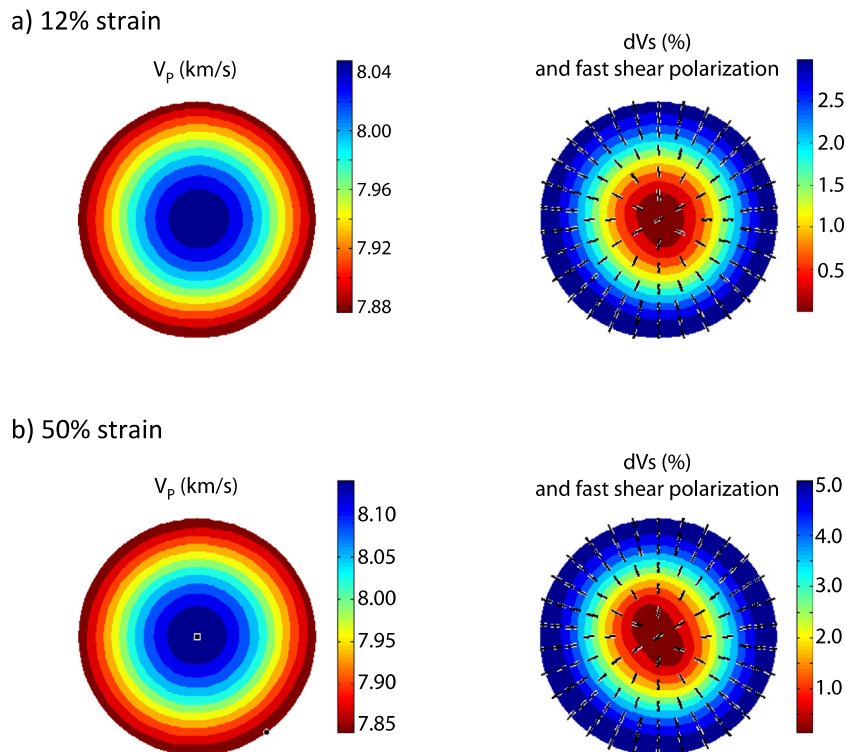


**Fig. 5.** Seismic velocities for a phase A polycrystal ( $C_{ij}$  at ambient pressure and temperatures) with (a) the experimental texture at 580 °C and 11 GPa, at 12% strain, and (b) a texture obtained from a VPSC simulation up to 50% deformation assuming the same slip systems and same strengthening properties as in (a) (same parameters as model E). The polycrystal was deformed in uniaxial geometry with the maximum compressive axis perpendicular to the projection plane shown here. (Color online.)

on the order of glaucophane-omphacite rocks with natural fabric that have about the same texture strength in Bezacier et al. (2010), lower than blueschists, and higher than anhydrous eclogites. This is a crude estimate relevant to regions of the slab that are moderately deformed.

In summary phase A will not create a seismic anisotropy as strong as its precursor serpentinized peridotite containing antigorite, and is less likely to help strain localization. How much it can be detected seismically among the other lithologies in a subducting slab does require further experimental studies, on samples deformed under large strains with simple shear geometry, and on multiphase aggregates.

## Acknowledgements

We acknowledge the use of the Institut National des Sciences de l'Univers (INSU) multi-anvil facility at the LMV in Clermont-Ferrand, for the sample synthesis, and the use of the INSU Raman facility at the LGLTPE in Lyon, for sample identifications. We thank D. Andrault and J.-L. Fruquière for their help at the multi-anvil facility, G. Montagnac for help at the Raman facility, C. Sanchez-Valle for discussions on phase A elasticity.

Portions of this work were performed at GeoSoilEnviroCARS (Sector 13), Advanced Photon Source (APS), Argonne National Laboratory. GeoSoilEnviroCARS is supported by the National Science Foundation – Earth Sciences (EAR-1128799) and Department of Energy–GeoSciences (DE-FG02-94ER14466). This research used resources of the Advanced Photon Source, a U.S. Department of Energy (DOE) Office of Science User Facility operated for the DOE Office of Science by Argonne National Laboratory under Contract No. DE-AC02-06CH11357.

This work was supported partly by the ANR project SUBDEF grant n° ANR-08-BLAN-0192 to B. Reynard (to E.A.), partly by the PNP INSU program (to N.H.), and partly by the European Research Council under the Seventh Framework Programme (FP7), ERC grant N° 290424 – RheoMan (to P.C. and K.G.). Deformation experiments were partially supported by EAR-0968456 and 1316276 (to Y.W.).

## Appendix A. Supplementary data

Supplementary data associated with this article can be found, in the online version, at <http://dx.doi.org/10.1016/j.pepi.2015.09.004>.

## References

- Amiguet, E., Reynard, B., Caracas, R., Van De Moortèle, B., Hilairt, N., Wang, Y., 2012. Creep of phyllosilicates at the onset of plate tectonics. *Earth Planet. Sci. Lett.* 345, 142–150. <http://dx.doi.org/10.1016/j.epsl.2012.06.033>.
- Bachmann, F., Hielscher, R., Schaeben, H., 2010. Texture analysis with MTEX – free and open source software toolbox. *Solid State Phenom.* 160, 63–68. <http://dx.doi.org/10.4028/www.scientific.net/SSP.160.63>.
- Bezacier, L., Reynard, B., Bass, J.D., Wang, J., Mainprice, D., 2010. Elasticity of glaucophane, seismic velocities and anisotropy of the subducted oceanic crust. *Tectonophysics* 494 (3–4), 201–210. <http://dx.doi.org/10.1016/j.tecto.2010.09.011>.
- Bloch, P.E., 1994. Projector augmented-wave method. *Phys. Rev. B* 50, 17953–17979.
- Bollinger, C., Merkel, S., Raterron, P., 2012. In situ quantitative analysis of stress and texture development in forsterite aggregates deformed at 6 GPa and 1373 K. *J. Appl. Crystallogr.* 45, 263–271. <http://dx.doi.org/10.1107/S002188981200516X>.
- Cover, M.F., Warschkow, O., Bilek, M.M.M., Mckenize, D.R., 2009. A comprehensive survey of M(2)AX phase elastic properties. *J. Phys. Condens. Matter* 21, 305403.
- Crichton, W.A., Ross, N.L., 2002. Equation of state of dense hydrous magnesium silicate phase A, Mg<sub>3</sub>Si<sub>2</sub>O<sub>8</sub>(OH)<sub>6</sub>. *Am. Mineral.* 87 (2–3), 333–338.
- Denoual, C., 2007. Modeling dislocation by coupling Peierls–Nabarro and element-free Galerkin methods. *Comput. Methods Appl. Mech. Eng.* 196, 1915–1923.
- Durinck, J., Legris, A., Cordier, P., 2005. Influence of crystal chemistry on ideal plastic shear anisotropy in forsterite: first principle calculations. *Am. Mineral.* 90 (7), 1072–1077.
- Eshelby, J.D., 1957. The determination of the elastic field of an ellipsoidal inclusion, and related problems. *Proc. R. Soc. Lond. A Math. Phys. Eng. Sci.*, 376–396 <http://dx.doi.org/10.1098/rspa.1957.0133> (The Royal Society).
- Hacker, B.R., Abers, G.A., Peacock, S.M., 2003. Subduction factory 1. Theoretical mineralogy, densities, seismic wave speeds, and H<sub>2</sub>O contents. *J. Geophys. Res. Solid Earth* 108 (B1), 2029. <http://dx.doi.org/10.1029/2001JB001127>.
- Hammersley, A., Svensson, S., Hanfland, M., Fitch, A., Hausermann, D., 1996. Two-dimensional detector software: from real detector to idealised image or two-theta scan. *Int. J. High Press. Res.* 14, 235–248.
- Hilairt, N., Reynard, B., Wang, Y., Daniel, I., Merkel, S., Nishiyama, N., Petitgirard, S., 2007. High-pressure creep of serpentine, interseismic deformation, and initiation of subduction. *Science* 318, 1910–1913. <http://dx.doi.org/10.1126/science.1148494>.
- Hilairt, N., Wang, Y., Sanehira, T., Merkel, S., Mei, S., 2012. Deformation of olivine under mantle conditions: an in situ high-pressure, high-temperature study using monochromatic synchrotron radiation. *J. Geophys. Res. Solid Earth* (1978–2012) 117 (B1).
- Horiuchi, H., Morimoto, N., Yamamoto, K., Akimoto, S., 1979. Crystal structure of 2Mg<sub>2</sub>SiO<sub>4</sub>·3Mg(OH)<sub>2</sub>, a new high-pressure structure type. *Am. Mineral.* 64, 593–598.
- Kagi, H., Parise, J.B., Cho, H., Rossman, G.R., Loveday, J.S., 2000. Hydrogen bonding interactions in phase A Mg<sub>3</sub>Si<sub>2</sub>O<sub>8</sub>(OH)<sub>6</sub> at ambient and high pressure. *Phys. Chem. Miner.* 27 (4), 225–233. <http://dx.doi.org/10.1007/s002690050251>.
- Komabayashi, T., Hirose, K., Funakoshi, K., Takafuji, N., 2005. Stability of phase A in antigorite (serpentine) composition determined by in situ X-ray pressure observations. *Phys. Earth Planet. Inter.* 151, 276–289. <http://dx.doi.org/10.1016/j.pepi.2005.04.002>.
- Kresse, G., Furthmüller, J., 1996a. Efficiency of ab-initio total energy calculations for metals and semiconductors using a plane-wave basis set. *Comput. Mater. Sci.* 6, 15–50.
- Kresse, G., Furthmüller, J., 1996b. Efficient iterative schemes for *ab initio* total-energy calculations using a plane-wave basis set. *Phys. Rev. B* 54, 11169–11186.
- Kresse, G., Hafner, J., 1993. Ab-initio molecular-dynamics for liquid-metals. *Phys. Rev. B* 47, 558–561.
- Kresse, G., Hafner, J., 1994. Ab-initio molecular-dynamics simulation of the liquid-metal amorphous-semiconductor transition in germanium. *Phys. Rev. B* 49, 14251–14269.
- Kresse, G., Joubert, D., 1999. From ultrasoft pseudopotentials to the projector augmented-wave method. *Phys. Rev. B* 59, 1758–1775.
- Lebensohn, R., Tomé, C., 1993. A self-consistent anisotropic approach for the simulation of plastic deformation and texture development of polycrystals: application to zirconium alloys. *Acta Metall. Mater.* 41, 2611–2624. [http://dx.doi.org/10.1016/0956-7151\(93\)90130-K](http://dx.doi.org/10.1016/0956-7151(93)90130-K).
- Lutterotti, L., Bortolotti, M., Ischia, G., Lonardelli, I., Wenk, H.-R., 2007. Rietveld texture analysis from diffraction images. *Z Kristallogr. Suppl. (Suppl. 26)*, 125–130.
- Mainprice, D., Ildefonse, B., 2009. *Seismic Anisotropy of Subduction Zone Minerals–Contribution of Hydrous Phases Subduction Zone Geodynamics*. Springer.
- Matthies, S., Vinel, G., 1982. On the reproduction of the orientation distribution function of texturized samples from reduced pole figures using the conception of a conditional ghost correction. *Phys. Status Solidi B* 112, K111–K114.
- Merkel, S., Hilairt, N., 2015. Multifit/polydefix: a framework for the analysis of polycrystal deformation using X-rays. *J. Appl. Crystallogr.* 48. <http://dx.doi.org/10.1107/S1600576715010390>.
- Metsue, A., Carrez, P., Denoual, C., Mainprice, D., Cordier, P., 2010. Peierls–Nabarro modelling of dislocations in diopside. *Phys. Chem. Miner.* 37, 711–720.
- Miyagi, L., Merkel, S., Yagi, T., Sata, N., Ohishi, Y., Wenk, H.-R., 2006. Quantitative Rietveld texture analysis of CaSiO<sub>3</sub> perovskite deformed in a diamond anvil cell. *J. Phys.: Condens. Matter* 18, S995. <http://dx.doi.org/10.1088/0953-8984/18/25/S07>.
- Monkhorst, H.J., Pack, J.D., 1976. Special points for Brillouin-zone integrations. *Phys. Rev. B* 13, 5188–5192.
- Mussi, A., Cordier, P., Frost, D.J., 2012. Crystal defects in dense hydrous magnesium silicate phase A deformed at high pressure: characterization by transmission electron microscopy. *Eur. J. Mineral.* 24, 429–438. <http://dx.doi.org/10.1127/0935-1221/2011/0024-2126>.
- Ohuchi, T., Kawazoe, T., Nishihara, Y., Nishiyama, N., Irifune, T., 2011. High pressure and temperature fabric transitions in olivine and variations in upper mantle seismic anisotropy. *Earth Planet. Sci. Lett.* 304 (1), 55–63.
- Peierls, R., 1940. *Proceedings of the Physical Society*, vol. 52. p. 34.
- Perdew, J.P., Wang, Y., 1992. Accurate and simple analytic representation of the electron-gas correlation-energy. *Phys. Rev. B* 45, 13244–13249.
- Pillon, L., Denoual, C., 2009. Inertial and retardation effects for dislocation interactions. *Phil. Mag.* 89, 127–141.
- Pillon, L., Denoual, C., Madec, R., Pellegrini, Y.P., 2006. Influence of inertia on the formation of dislocation dipoles. *J. Phys. IV* 134, 49–54.
- Pillon, L., Denoual, C., Pellegrini, Y.P., 2007. Equation of motion for dislocations with inertial effects. *Phys. Rev. B* 76, 224105.
- Poli, S., Schmidt, M., 1997. The high-pressure stability of hydrous phases in orogenic belts: an experimental approach on eclogite-forming processes. *Tectonophysics* 273, 169–184. [http://dx.doi.org/10.1016/S0040-1951\(96\)00293-4](http://dx.doi.org/10.1016/S0040-1951(96)00293-4).

- Sanchez-Valle, C., Sinogeikin, S.V., Smyth, J.R., Bass, J.D., 2006. Single-crystal elastic properties of dense hydrous magnesium silicate phase A. *Am. Mineral.* 91, 961–964. <http://dx.doi.org/10.2138/am.2006.2193>.
- Sanchez-Valle, C., Sinogeikin, S.V., Smyth, J.R., Bass, J.D., 2008. Sound velocities and elasticity of DHMS phase A to high pressure and implications for seismic velocities and anisotropy in subducted slabs. *Phys. Earth Planet. Inter.* 170, 229–239. <http://dx.doi.org/10.1016/j.pepi.2008.07.015>.
- Uchida, T., Funamori, N., Yagi, T., 1996. Lattice strains in crystals under triaxial stress field. *J. Appl. Phys.* 80 (2), 739–746. <http://dx.doi.org/10.1063/1.362920>.
- Walker, A.M., Wookey, J., 2012. MSAT-A new toolkit for the analysis of elastic and seismic anisotropy. *Comput. Geosci.* 49, 81–90. <http://dx.doi.org/10.1016/j.cageo.2012.05.031>.
- Wallace, D.C., 1970. *Thermoelastic theory of stressed crystals and higher-order elastic constants*. In: Henry Ehrenreich, F.S., David, T. (Eds.), *Solid State Physics*. Academic Press.
- Wang, Y., Durham, W.B., Getting, I.C., Weidner, D.J., 2003. The deformation-DIA: a new apparatus for high temperature triaxial deformation to pressures up to 15 GPa. *Rev. Sci. Instrum.* 74, 3002–3011. <http://dx.doi.org/10.1063/1.1570948>.